



OPEN

SUBJECT AREAS:

BIOCATALYSIS

NANOPARTICLES

BIOANALYTICAL CHEMISTRY

BIOSENSORS

Ternary Composite of Hemin, Gold Nanoparticles and Graphene for Highly Efficient Decomposition of Hydrogen Peroxide

Xincong Lv¹ & Jian Weng^{1,2}Received
11 September 2013Accepted
4 November 2013Published
21 November 2013Correspondence and
requests for materials
should be addressed to
J.W. (jweng@xmu.
edu.cn)¹Department of Biomaterials, College of Materials, Xiamen University, Xiamen 361005, P.R. China, ²ShenZhen Research Institute of Xiamen University, Shenzhen 518057, China.

A ternary composite of hemin, gold nanoparticles and graphene is prepared by a two-step process. Firstly, graphene-hemin composite is synthesized through π - π interaction and then hydrogen tetrachloroauric acid is reduced *in situ* by ascorbic acid. This ternary composite shows a higher catalytic activity for decomposition of hydrogen peroxide than that of three components alone or the mixture of three components. The Michaelis constant of this composite is 5.82 times lower and the maximal reaction velocity is 1.81 times higher than those of horseradish peroxidase, respectively. This composite also shows lower apparent activation energy than that of other catalysts. The excellently catalytic performance could be attributed to the fast electron transfer on the surface of graphene and the synergistic interaction of three components, which is further confirmed by electrochemical characterization. The ternary composite has been used to determine hydrogen peroxide in three real water samples with satisfactory results.

Natural enzymes have been extensively investigated and widely applied because of their excellent properties, including high substrate specificity and catalytic efficiency. However, high costs of preparation, purification and storage restrict their widespread applications. Therefore, great attention has been paid to the construction and discovery of novel enzyme mimetics. Among them, many peroxidase mimetics, such as Fe₃O₄ nanoparticles¹, graphene oxide (GO)², porphyrin³, *etc.*, have been successfully developed and used for H₂O₂ detection. Hemin (iron protoporphyrin) is the active center of heme-proteins, such as cytochromes, peroxidases, myoglobins, and hemoglobins, which has the peroxidase-like activity⁴. However, its catalytic activity and stability is inferior to natural enzymes⁵. Therefore, in recent years, large numbers of reports have dedicated to improve the performance of hemin. For example, hydrogel-embedded hemin⁶ and more elaborate hemin complexes⁷. They all show activities significantly better than that of hemin, however, still orders of magnitude inferior to natural enzymes, not to mention the difficulties in the synthesis of such kinds of complex hemin conjugates. Therefore, a simple and efficient way to promote ability of hemin still remains a challenge.

Graphene, a new class of two-dimensional carbon nanostructure, possesses unique electronic, optical and mechanical properties⁸⁻¹⁰. In addition, given its large specific surface area¹¹ and high adsorption capacity, graphene and its derivatives can be used as valuable substrates to interact with various species. These composites can then be used in solar cells¹², memory devices¹³, and even drug delivery¹⁴. Most recently, Qu *et al.*² reported that GO had an intrinsic enzyme mimetic activity similar to that of natural peroxidases such as horseradish peroxidase (HRP). It also has been found that graphene-hemin composite through π - π interaction has a higher catalytic ability for decomposition of hydrogen peroxide⁵.

Noble-metal nanoparticles (NPs) have received tremendous interest, especially because of their fascinating catalytic activity, and potential applications in a wide range such as surface plasmonics¹⁵, biosensor¹⁶, diagnostics¹⁷, and catalysis¹⁸. Recently, Li and co-workers reported that the positively-charged gold NPs exhibited highly intrinsic peroxidase-like activity¹⁹. In addition, Xu and co-workers found that gold NPs bound on microgel particles could enhance the performance of HRP²⁰. There are also some reports that a low concentration of silver NPs (or gold NPs) can improve the activity of HRP²¹.

Although the synergistic effect of the two materials to promote the decomposition of hydrogen peroxide was reported by several research groups, there are still some problems including low catalytic activity and complicated



synthetic steps. In this report, we prepared the hemin-graphene-gold (H-RGO-Au) ternary composite by a simple method. Firstly, Hemin-graphene nanosheet (H-RGO) was synthesized by simple wet-chemical strategy through the π - π interaction. Then hydrogen tetrachloroauric acid was reduced *in situ* on the surface of H-RGO by ascorbic acid. To our surprise, this new composite has superior performance for decomposition of hydrogen peroxide than that of three components alone or the mixture of three components with the same concentration. Moreover, it also shows higher catalytic activity than that of HRP. This excellent performance is attributed to the high electron transfer rate of graphene and the synergistic interaction of three components. On the basis of these findings, we have, for the first time, employed the composite as a novel peroxidase mimetic to offer a simple, sensitive and selective colorimetric method for H_2O_2 detection in real water samples.

Results

Synthesis and structure characterization of H-RGO-Au. GO was prepared according to the modified Hummer's method^{13,14,22}. Two steps were adopted to synthesize H-RGO-Au. Firstly, H-RGO was synthesized by refluxing a mixture of hemin and GO in ammonia in the presence of hydrazine. In this process, GO was reduced by hydrazine and formed a composite of H-RGO by π - π interaction. In the second step, the ternary composite of H-RGO-Au was obtained through reducing hydrogen tetrachloroauric acid *in situ* (Fig. 1). The resulted suspension of H-RGO-Au has a good stability in a certain range of pH from 3 to 9 (Fig. S1a). However, when the pH of suspension was altered to 2, the suspension became agglomerated gradually, which could be attributed to the surface electrostatic effect. As the pH is adjusted to 2, the zeta potential of H-RGO-Au changes into positive and this electrostatic repulsion is weakened. Hence, the

suspension is unstable and finally complete precipitation. The zeta potential of as-obtained H-RGO-Au is negative in the pH range from 3 to 9 which leads to a good dispersion due to the intermolecular repulsion force (Fig. S1b).

Fig. 2a shows the transmission electron microscopy (TEM) image of the synthesized GO. It can be seen that there is a layer of GO with a wrinkled and folded morphology. The atomic force microscopy studies have shown that only a single layer of GO was formed²². In addition, selected-area electron diffraction (SAED) is performed to determine its crystalline nature (Fig. 2a inset). The well-defined hexagonal diffraction pattern, which is similar to that of single-layer graphene prepared by manual peeling off from graphite, confirms the crystalline structure of graphene-sheet²³. Fig. 2b shows TEM image of H-RGO. Obviously, we can see some aggregated hemin particles on the surface of RGO and the surface of RGO is not smooth due to the adsorbed hemin. Furthermore, the SAED of H-RGO (Fig. 2b inset) shows well-defined diffraction pattern, which further indicates the crystalline nature of the RGO. Intensity difference in the diffraction spots suggests the formation of few-layered RGO due to its intrinsic nature to form stacks²⁴. The elements of the materials in Fig. 2b were further investigated by X-ray energy dispersive spectroscopy (EDS). Compared with GO (Fig. S2a), H-RGO (Fig. S2b) shows a small amount of Fe and Cl, which indicates the existence of hemin on the surface of the RGO. Fig. 2c show TEM image of H-RGO-Au. The gold NPs are dispersed on the surface of H-RGO and the measured size is about 8 ± 3 nm based on size distribution in Fig. S3 a-d. The SAED pattern acquired from the sample is shown as an inset in Fig. 2c. We identified the structure as face centered cubic (fcc) gold space group (JCPDS card NO: 65-2870) by indexing the diffraction pattern. At the same time, we can also see the diffraction spots of few-layered RGO. From high-resolution TEM (Fig. 2d), we find the

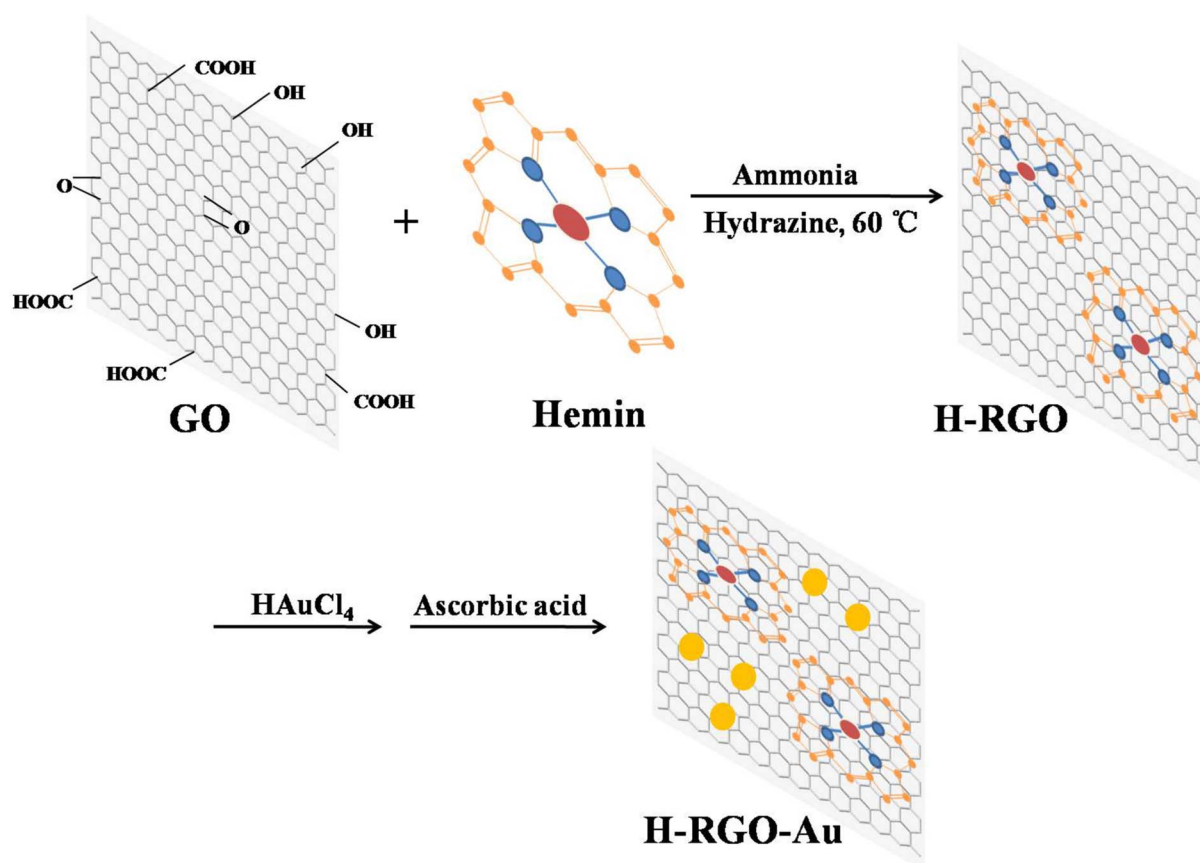


Figure 1 | Schematic for the preparation of H-RGO and H-RGO-Au. Hemin is adsorbed on the surface of graphene due to the π - π interaction, then hydrogen tetrachloroauric acid is reduced *in situ* by ascorbic acid.

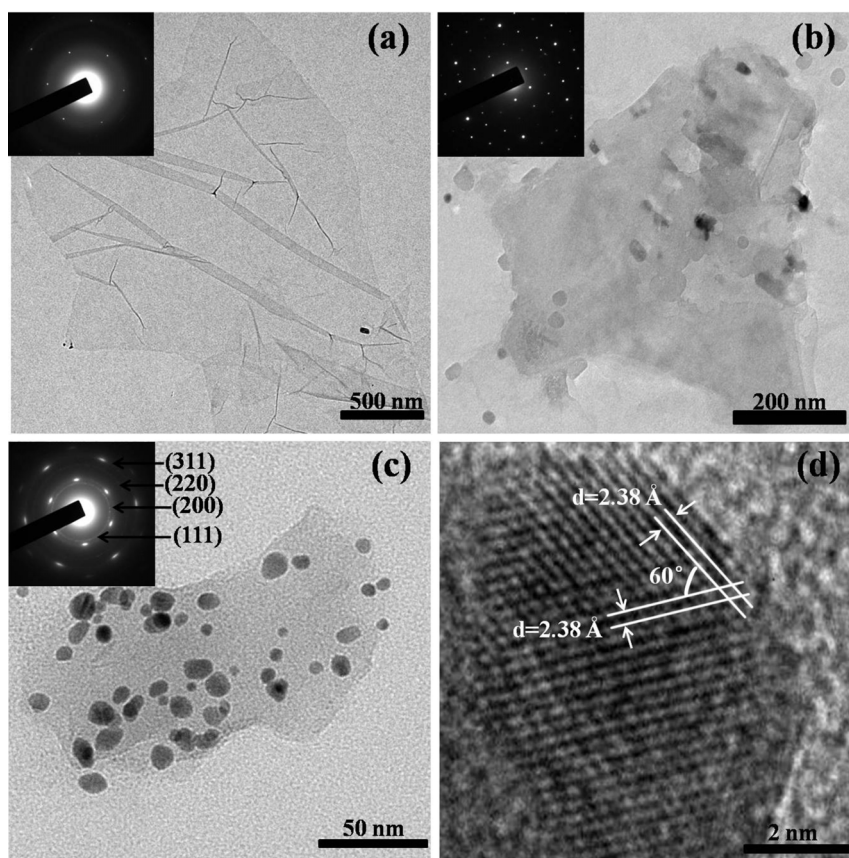


Figure 2 | TEM images of the as-synthesized nanomaterials. (a) GO. Inset shows the corresponding SAED of GO. (b) H-RGO. Inset is SAED of H-RGO. (c) H-RGO-Au. Inset is SAED of H-RGO-Au. (d) High-resolution TEM of H-RGO-Au. The loading of Au nanoparticles is 32 wt%.

detailed lattice fringe oblique intersection at an angle of 60° of the gold crystallites. In addition, interplanar spacings were measured to be 0.21 and 0.238 nm (Fig. S3e and f), which corresponds to (200) and (111) planes in gold, respectively. The EDS of H-RGO-Au further confirms that we obtained the composite of H-RGO-Au (Fig. S2c).

Shown in Fig. 3a is the ultraviolet-visible (UV-vis) absorption spectra of aqueous dispersions of GO, hemin, H-RGO and H-RGO-Au. GO exhibits a strong peak centered at 233 nm and a shoulder peak at 300 nm corresponding to π - π^* transitions of aromatic C=C band and n - π^* transitions of C=O band, respectively²⁵. On the other hand, the peak at 233 nm red-shifts to 262 nm, the shoulder peak at 300 nm disappears, which indicates that GO was reduced by hydrazine and the restoration of the π -conjugation network within RGO during the synthesis of H-RGO. In the absence of RGO, the spectrum of hemin solution contains a strong peak at 388 nm attributed to the Soret band of hemin, as well as a group of weak peaks between 500 and 700 nm ascribed to the Q-bands of hemin. In the presence of RGO, maximum of the Soret band of hemin red-shifts from 388 to 413 nm, which could be attributed to the adsorption of hemin molecule on RGO driven by π - π stacking interaction between the porphyrin moiety and RGO. In addition, there is a new absorption peak at about 541 nm for H-RGO-Au, corresponding to the surface plasmon absorption of gold NPs. Fig. 3b further explored the effect of gold concentration on the composite structure. With increasing concentration of HAuCl_4 , more gold NPs were produced. Therefore, the absorption peak intensity at 541 nm gradually increased. The absorption peak intensity of RGO at 262 nm also increased which could be attributed to the further reduction of graphene by ascorbic acid²⁶. On the other hand, there is a new absorption peak at 229 nm especially in high

concentration of gold NPs which is considered to be the oxidation products of ascorbic acid containing oxygen functional groups²⁷. The absorption of hemin molecule at 413 nm gradually disappeared due to the increasing concentrations of the other two components to cover up this peak. All results indicate that there would be a strong interaction among three components.

Fig. 4a shows the XRD patterns of the as-synthesized GO, H-RGO and H-RGO-Au, all of them show a broad peak around 24.3° which corresponds to the characteristic diffraction peak (002) of the hexagonal structure of graphene. In addition, there are five strong diffraction peaks in H-RGO-Au which could be indexed to the (111), (200), (220), (311) and (222) planes of the Au NPs. Compared with the pattern of bulk Au from the Joint Committee on Powder Diffraction Standards (JCPDS), the diffraction peaks from the synthesized Au NPs are located in the same angles, strongly indicating the formation of Au NPs. Based on the Scherrer formula: $D = K\lambda/\beta\cos\theta$, where D is the mean diameter of gold NPs, β is the full-width at half-maximum of the peak at 2θ , K is shape-dependent Scherrer's constant of 0.94 and λ is radiation wavelength (1.5406 Å). The calculated size of gold NPs is 8.2 nm, which is consistent with the measured size by TEM (8 ± 3 nm).

Raman spectroscopy is widely used to detect the ordered and disordered crystalline structure of graphene. Fig. 4b shows the Raman spectra of GO, H-RGO and H-RGO-Au. For all three samples, the two peaks at about 1347 and 1588 cm^{-1} can be assigned to the D- and G-band, respectively. The D-band is related to the vibrations of sp^3 carbon atoms of disordered graphene nanosheets, while the G-band arises from vibrations of sp^2 carbon atom domains of graphite. From Fig. 4b, the intensity ratios of D- and G-bands (I_D/I_G) from H-RGO and H-RGO-Au are obviously larger than that of GO (0.973 in GO, 0.991 in H-RGO and 1.005 in H-RGO-Au), which

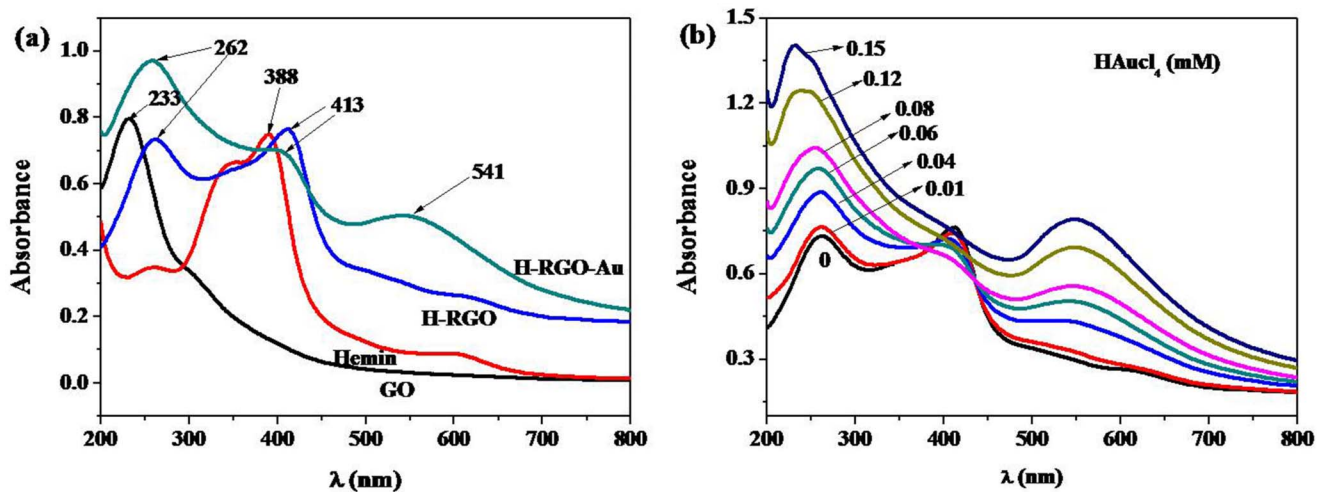


Figure 3 | UV-vis absorption spectra of the as-synthesized nanomaterials. (a) UV-vis absorption spectra of GO, Hemin, H-RGO and H-RGO-Au. (b) UV-vis absorption spectra of H-RGO-Au with different initial concentrations of HAuCl_4 .

confirms that most of the oxygenated groups would have been removed during the reduction process²⁸. In addition, D- and G-bands in H-RGO and H-RGO-Au produce a small red shift compared with GO, which strongly suggests an interaction between graphene and the other two components.

Peroxidase-like activity of H-RGO-Au. It is well known that hemin is the activate site in peroxidase and exhibits the peroxidase-like activity⁴. Therefore, we further investigate the catalytic properties of H-RGO, H-Au and H-RGO-Au. The peroxidase-like activity was evaluated in the catalytic oxidation of peroxidase substrate 3,3',5,5'-tetramethylbenzidine (TMB). The TMB cation free radical, a one-electron oxidation product, would be formed with exposure of TMB to peroxidase and H_2O_2 . It is responsible for the blue color (maximum absorbance at 652 nm) that develops during TMB oxidation²⁹. The catalytic reaction can be detected by monitoring absorbance change of oxidation products of TMB at 652 nm.

Fig. 5a is the absorbance change with time in the mixture of TMB, H_2O_2 and H-RGO-Au. The increase in absorbance at 652 nm is considered to be gradually increased oxidation product of TMB. Fig. 5b demonstrates that both of H_2O_2 and as-obtained H-RGO-Au cannot alone oxidize TMB efficiently. Therefore, TMB oxidation is resulted from the decomposition of H_2O_2 by as-obtained H-RGO-

Au. In order to compare the effect of different catalysts, we measure the time-dependent absorbance curve under the same condition. Fig. 5c illustrates the catalytic activity of different materials with the same concentration. The hemin itself has a higher catalytic activity than that of RGO and gold NPs. There is also a weak synergy between gold and RGO which has been reported by other researchers³². Furthermore, the hemin modified with gold NPs or RGO has a higher catalytic activity than that of hemin itself, which could be attributed to the synergistic effect between hemin molecule and nanomaterials^{5,21}. Much to our surprise, gold and RGO can also work together to promote the performance of hemin due to the synergistic effect of three components which will be confirmed in follow. Fig. 5d compares the catalytic activity of ternary composites, simple mixing of three components and three components alone. This experiment was performed according to the following steps. First, the content of hemin and gold NPs in H-RGO-Au is calculated to be about 11 wt% and 32 wt%, respectively, which can be obtained by thermal gravimetric analysis (TGA) (Fig. S4a and b). Then a simple mixing of three components (H + RGO + Au) is obtained by only mixing of 11 wt% hemin, 32 wt% gold NPs and 57 wt% RGO in solution which the final concentration is same as H-RGO-Au. At last, the catalytic properties of 11 wt% hemin, 32 wt% gold NPs and 57 wt% RGO were investigated, respectively. Obviously, we find from the inset that the absorbance at 652 nm for H-RGO-Au has a highest value

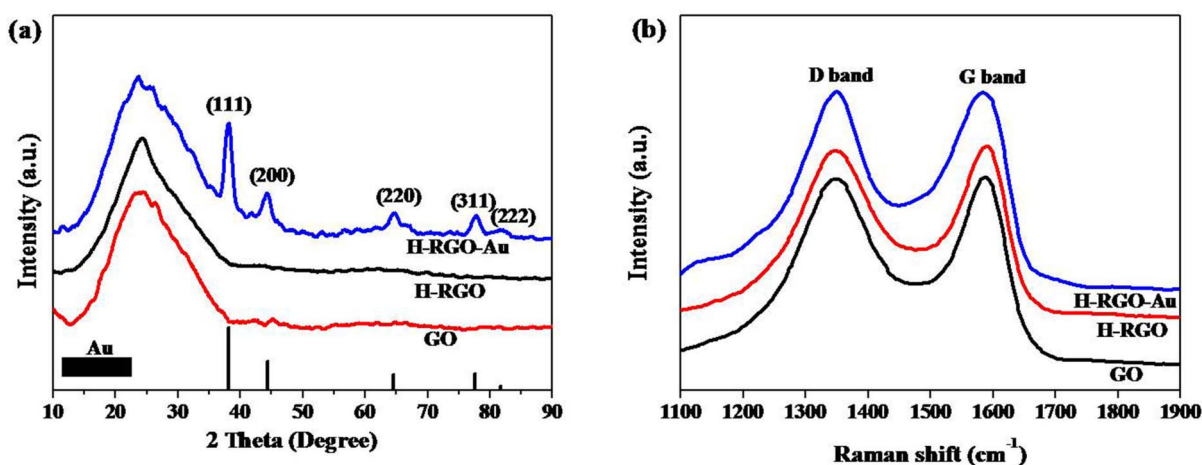


Figure 4 | Structural characterization of the as-synthesized nanomaterials. (a) XRD patterns of the as-synthesized GO, H-RGO and H-RGO-Au. For comparison, the JCPDS pattern of bulk Au is also included. (b) Raman spectra of GO, H-RGO and H-RGO-Au.

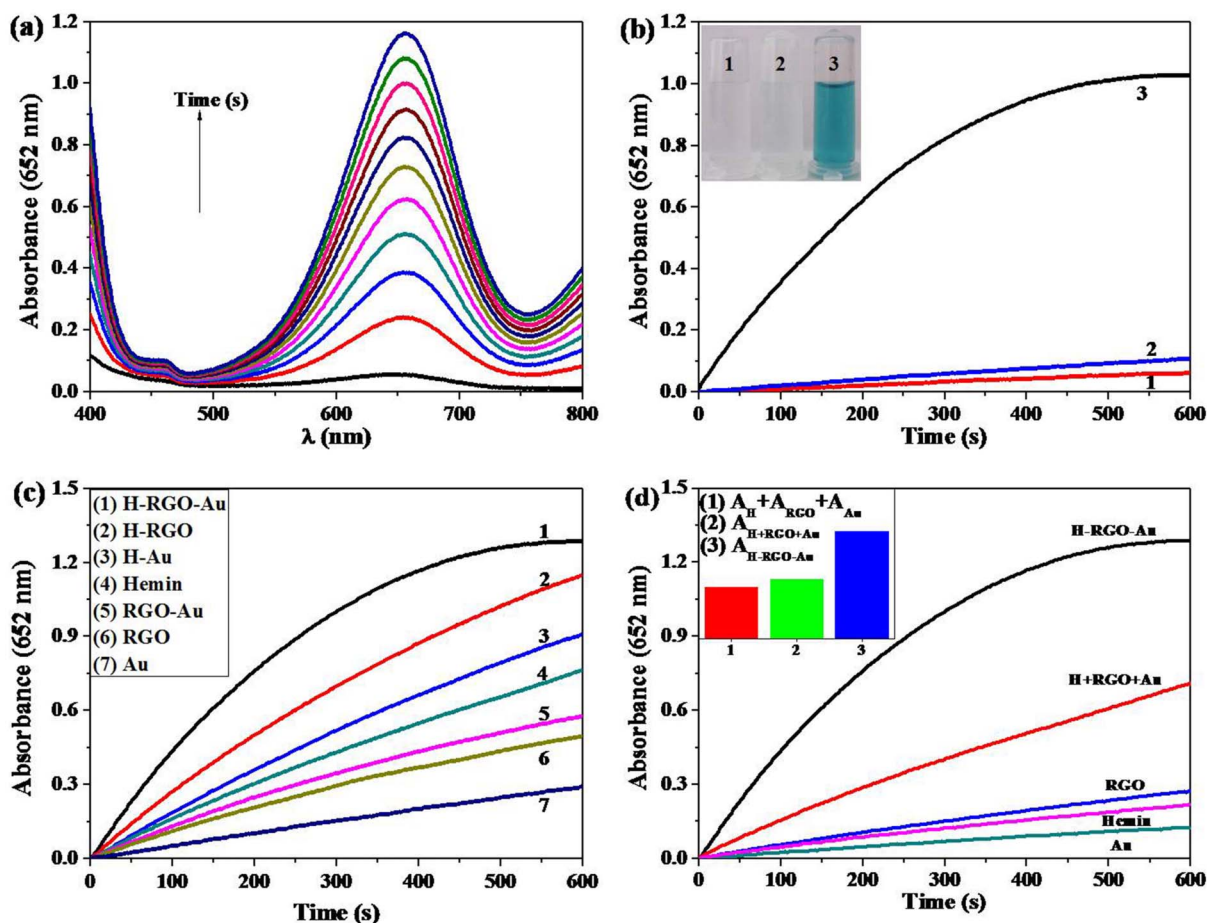


Figure 5 | Peroxidase-like activity of as-synthesized nanomaterials. (a) UV-vis spectra for the mixed solution of TMB and H_2O_2 obtained at same intervals after the addition of as-obtained H-RGO-Au. (b) The time-dependent absorbance changes at 652 nm of 600 μL TMB reaction solutions in the presence of (1) H-RGO-Au, (2) H_2O_2 , (3) H-RGO-Au and H_2O_2 , respectively; Inset is the photograph of above three solutions after 10 min. (c) The time-dependent absorbance change at 652 nm of different materials with the same concentration. (d) The time-dependent absorbance change at 652 nm of H-RGO-Au, simple mixing of three components and addition of three components alone. Inset is the value of absorbance after reaction ten minutes.

than that of addition of three components alone ($A_{\text{Hemin}} + A_{\text{RGO}} + A_{\text{Au}}$) or simple mixing of three components ($A_{\text{Hemin}} + A_{\text{RGO}} + A_{\text{Au}}$). In addition, the value of $A_{\text{Hemin}} + A_{\text{RGO}} + A_{\text{Au}}$ is a little higher than that of $A_{\text{Hemin}} + A_{\text{RGO}} + A_{\text{Au}}$ due to a weak synergy when three components are simply mixed. The result shows that there might be strongly synergistic effect of three components to improve the catalytic activity of H-RGO-Au.

To further explore the effect of RGO and gold NPs on the catalytic properties of H-RGO-Au, a series of experiments were performed. Fig. S5a is the time-dependent absorbance changes of H-RGO-Au with different concentrations of GO and the constant concentrations of HAuCl_4 . Fig. S5b demonstrates that the optimally initial concentration of GO in H-RGO-Au is 0.25 mg mL^{-1} . Fig. S5c is the time-dependent absorbance changes of H-RGO-Au with different loading of gold nanoparticles in H-RGO-Au. and the constant concentrations of GO. Fig. S5d shows that the optimal loading of gold NPs in H-RGO-Au is 32 wt%.

Fig. S6a demonstrates that the reaction rate increases with the H-RGO-Au concentration increasing to 0.5 $\mu\text{g mL}^{-1}$. Similar to peroxidase, H-RGO-Au catalytic activity is dependent on pH, temperature, and H_2O_2 concentration. From Fig. S6b, c and d, the optimal pH, temperature, and H_2O_2 concentration are pH 4.0, 40°C, and 200 mM, respectively, which are close to the values for natural enzyme HRP¹.

For further analyzing the catalytic mechanism and acquiring kinetic parameters, the catalytic activity of H-RGO-Au was studied by

enzyme kinetics experiments with H_2O_2 and TMB as substrates. A series of experiments were performed by changing the concentration of one substrate and fixing the concentration of another (Fig. 6a and d). In a certain range of substrate concentrations, typical Michaelis-Menten curves can be obtained as shown in Fig. 6b and e for TMB and H_2O_2 , respectively. Based on the different oxidation rates with variable substrate concentrations, a Lineweaver-Burk plot can be obtained with a nearly perfect linear relationship (Fig. 6c and f), from which the important kinetic parameters such as K_m and V_{max} can be derived (Table 1). K_m was identified as an indicator of enzyme affinity to substrates. A low K_m represented a strong affinity and vice versa³⁰. By comparing the apparent kinetic parameters, the apparent K_m value of H-RGO-Au with H_2O_2 as the substrate is 1.6 times lower than that of hemin, 49.7 times lower than that of Fe_3O_4 magnetic nanoparticles and 1.2 times lower than that of HRP. The K_m value of H-RGO-Au with TMB as the substrate is also 10.14 times lower than that of hemin, 1.32 times lower than that of Fe_3O_4 MNPs and 5.82 times lower than that of HRP. In addition, we calculate the equivalent data for HRP by calculating the kinetic parameters ratio between different materials and HRP (Table 1 brackets). The K_m of H-RGO-Au with TMB as substrate is lower than that of other catalysts, which could be attributed to high surface-to-volume ratios of RGO that could absorb TMB efficiently³¹. In addition, graphene could serve as a support to anchor hemin and gold NPs and restrict the substrates in a nanoscale region, which could greatly enhance the catalytic activity of H-RGO-Au³².

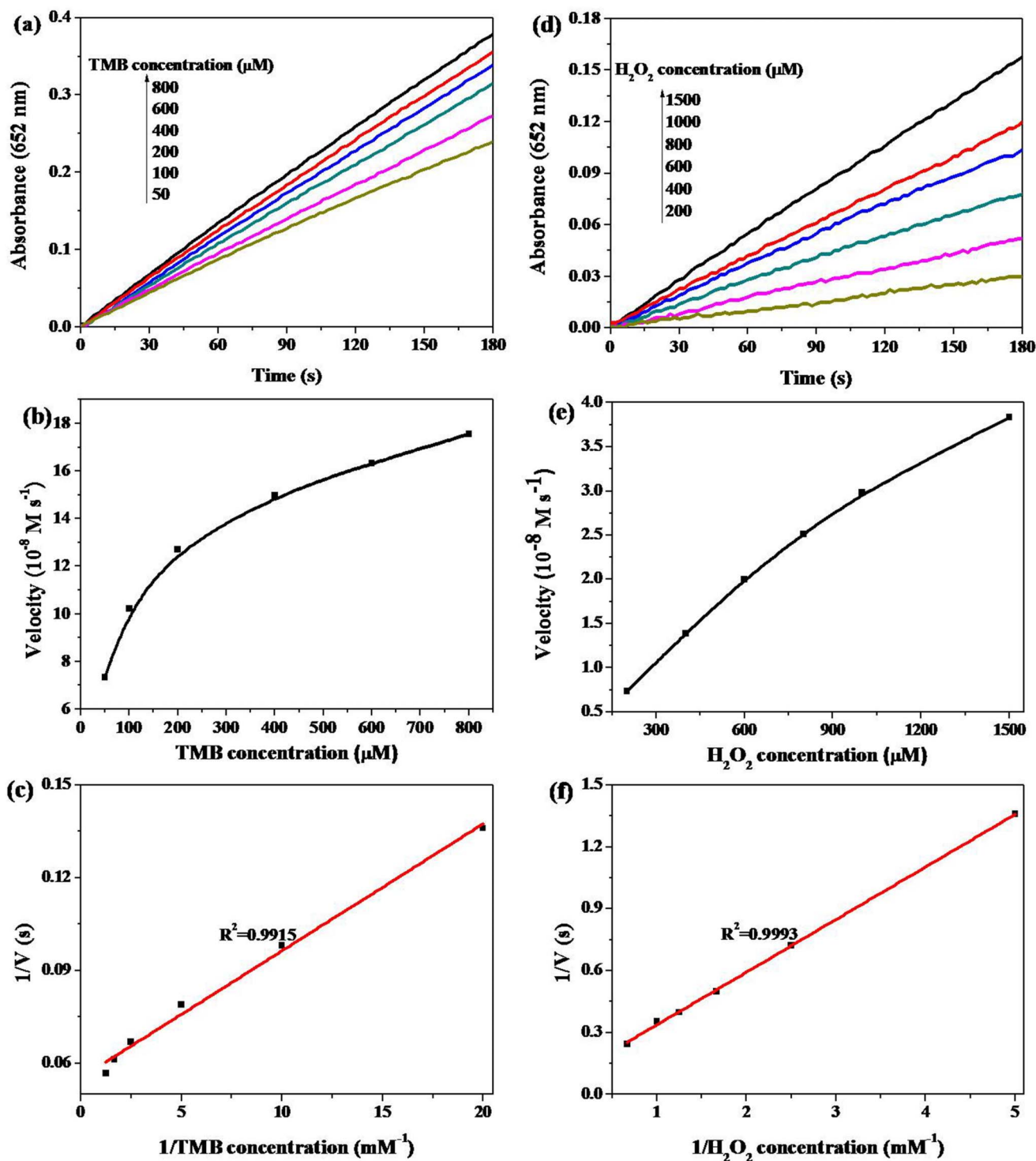


Figure 6 | Steady-state kinetic assay of H-RGO-Au. (a), (d) Time-dependent absorbance changes at 652 nm of TMB reaction solutions catalyzed by the H-RGO-Au in the presence of different concentrations of TMB or H₂O₂. (b), (e) The velocity (v) of the reaction changes in the presence of different concentrations of TMB or H₂O₂. (c), (f) Double reciprocal plots of activity of H-RGO-Au in the presence of different concentrations of TMB or H₂O₂. Experiments were carried out in 0.02 M acetic acid-sodium acetate buffer (pH 4.0) using 0.5 μg mL⁻¹ H-RGO-Au at 25°C. (a), (b), (c) H₂O₂ concentration was fixed at 10 mM and the TMB concentration was varied. (d), (e), (f) TMB concentration was fixed at 600 μM and the H₂O₂ concentration was varied.

Furthermore, the V_{\max} of H-RGO-Au is higher than that of the other reported catalysts. Taken together, originating from the synergetic effect among RGO, gold NPs and hemin, the materials indeed showed an higher peroxidase-like activity than that of other reported catalysts.

It is necessary to further investigate the thermodynamics of the catalytic reaction for H₂O₂ by H-RGO-Au. The catalytic reaction is carried out at different temperatures from 25°C to 39°C by monitoring absorbance change of the oxidation product of TMB at 652 nm. Then we can obtain the value of rate constant (k) through fitting the


Table 1 | Kinetic parameters for the TMB oxidation reaction catalyzed using different catalysts. Brackets are the equivalent data for HRP

Catalysts	K_m/mM^{-1}		$V_{\text{max}}/10^{-8} \text{ M s}^{-1}$	
	TMB	H_2O_2	TMB	H_2O_2
RGO-Au-Hemin	0.074 (0.172)	3.1 (0.838)	18.1 (1.81)	12.1 (1.39)
Hemin	0.75 (1.74)	5.11 (1.38)	6.2 (0.62)	5.6 (0.643)
Fe_3O_4 MNPs ¹	0.098 (0.227)	154 (41.6)	3.44 (0.344)	9.78 (1.12)
HRP ¹	0.431 (1)	3.7 (1)	10.0 (1)	8.71 (1)

absorbance data to pseudo-first-order kinetics (Fig. S7a, b, c). The result was listed in Table 2, we can find that the rate constant increases with increasing temperature. Furthermore, the apparent activation energy (E_a) and the pre-exponential factor (A) can be obtained from the slope and intercept of the linear $\ln(1/k)$ vs $1000/T$ dependence (slope = E_a/R , intercept = $-\ln A$) based on Arrhenius equation (Fig. S7d). The E_a of this system is calculated to be $20.37 \text{ kJ mol}^{-1}$, which is lower than that of few-layer graphene (28 kJ mol^{-1})³³, iron oxide (60 kJ mol^{-1})³⁴, bimetallic Pt-Pd (36.4 kJ mol^{-1})³⁵ and ferrihydrites ($76.13 \text{ kJ mol}^{-1}$)³⁶, indicating a high catalytic activity for the as-prepared H-RGO-Au. The entropy of activation (ΔS) can also be obtained on the basis of the value of pre-exponential factors³⁷. The calculated values were listed in Table 2.

To further explore the mechanism of high catalytic activity, we have designed a series of experiments. Firstly, we compared the catalytic activity of H-RGO-Au with hemin and H-GO-Au which is prepared in the same way like H-RGO-Au except no adding hydrazine (Fig. S8). The peroxidase catalytic activity of H-RGO-Au is 1.92 times higher than that of hemin and 1.14 times higher than that of H-GO-Au with the same concentration of $0.5 \mu\text{g mL}^{-1}$.

Based on the above discovery, we speculate that the high catalytic activity of H-RGO-Au would result from the high electron transfer rate of RGO^{38–40}. Therefore, we further use the electrochemical experiments to support our speculation. Firstly, the electrochemical properties of H-RGO-Au, H-GO-Au and hemin were investigated by cyclic voltammetry technology. The cyclic voltammograms (CVs) of H-RGO-Au, H-GO-Au and hemin-modified gold electrodes in phosphate buffer solution containing $5 \text{ mM K}_3\text{Fe}(\text{CN})_6$ were showed in Fig. 7a. H-RGO-Au-modified electrode has a highest current intensity and a lowest peak-to-peak separation (H-RGO-Au is 76 mV , H-GO-Au is 96 mV and hemin is 116 mV) than that of others. The result indicates faster electron-transfer kinetics at H-RGO-Au-modified electrode than that of others^{41,42}.

The effect of scan rates on the electrochemical response of $\text{K}_3\text{Fe}(\text{CN})_6$ at the different electrodes was investigated for further understanding the catalytic mechanism of H-RGO-Au. In Fig. S9 a–c, CVs of the $\text{K}_3\text{Fe}(\text{CN})_6$ were performed at different electrodes by changing scan rates from 0.05 to 5 V s^{-1} . With the square root of scan rate increasing, both of anodic and cathodic peak currents increase linearly (Fig. S9 d–f). Therefore, the electrochemically active surface area can be calculated roughly from the formula listed in Methods. The electrochemically active surface area of H-RGO-Au (0.034 cm^2) is nearly 1.42 times higher than that of H-GO-Au (0.024 cm^2) and 2 times higher than that of hemin (0.017 cm^2). Therefore, the higher conductivity of H-RGO-Au than that of H-GO-Au and hemin might result from the high surface area. On the other hand, we also investigated the electrocatalytic activity of H_2O_2

by H-RGO-Au, H-GO-Au and Hemin (Fig. 7b). Among three different electrodes, H-RGO-Au-modified electrode shows a higher current intensity than that of others, which also means that it had a higher catalytic activity toward H_2O_2 than that of H-GO-Au and hemin.

CVs at increasing scan rates from 0.1 to 3 V s^{-1} were also recorded to investigate electrocatalytic activity of H_2O_2 by different modified electrodes (Fig. S10 a–c). By comparing and calculating ratio of the slope of current vs square root of scan rate (Fig. S10 d–f), the electrode surface area of H-RGO-Au is about 1.7 times higher than that of H-GO-Au and 2.07 times higher than that of hemin, which further confirms that H-RGO-Au would have higher conductivity than that of H-GO-Au and hemin.

Application of H-RGO-Au. On the basis of the intrinsic peroxidase-like property of H-RGO-Au, we developed a simple colorimetric method to detect H_2O_2 . The concentration response curve of H_2O_2 to the absorbance of TMB is presented in Fig. S11a. A linear relationship is established in the range of 0.05 – $40 \mu\text{M}$ with a correlation coefficient of 0.9940 (Fig. S11b). The detection limit of H_2O_2 was found to be about 5 nM (the signal-to-noise ratio is two), which is lower than that of Se/Pt composite ($3.1 \mu\text{M}$)⁴³, Au-graphene-HRP ($1.7 \mu\text{M}$)⁴⁴, graphene and ZnO composites-based amperometric biosensor ($0.6 \mu\text{M}$)⁴⁵, and graphene-modified electrode ($0.11 \mu\text{M}$)⁴⁶.

Hydrogen peroxide detection is a common analysis in the clinic and industry⁴⁷. Here, H-RGO-Au was also used to determine hydrogen peroxide concentration in three real water samples. Three parallel experiments were performed for each measurement. Standard addition method was carried out to confirm the feasibility of the system. The results of the determination and recovery are shown in Table 3. It shows that the average recoveries for hydrogen peroxide at three spiked levels with standard addition method ranged from 98.7 to 103.1% . Table 3 also shows the precision of the method. The relative standard deviation (RSD) values of the measurements were obtained at each concentration level. Good recovery and precision of hydrogen peroxide determination suggest that the peroxidase-like activity-based colorimetric method might be used to analyze hydrogen peroxide in water samples.

Discussion

We have successfully prepared H-RGO-Au and found that it could exhibit excellent peroxidase-like activity due to the synergistic interaction of three components. The UV-vis spectroscopy, XRD, and Raman of H-RGO-Au indicate that there would be a strong interaction among three components, which might enhance the decomposition of hydrogen peroxide. The comparative experiments for

Table 2 | Summary of the reaction rate constant (k), activation energy (E_a), pre-exponential factors (A), and the entropy of activation (ΔS)

T (K)	$1000 (K^{-1})$	$k (\text{min}^{-1})$	$E_a (\text{kJ mol}^{-1})$	$A (\text{min}^{-1})$	$\Delta S (\text{J mol}^{-1} K^{-1})$
298.15	3.354	0.236 ± 0.01	20.37	871	56.29
305.15	3.277	0.281 ± 0.013			
312.15	3.204	0.341 ± 0.015			

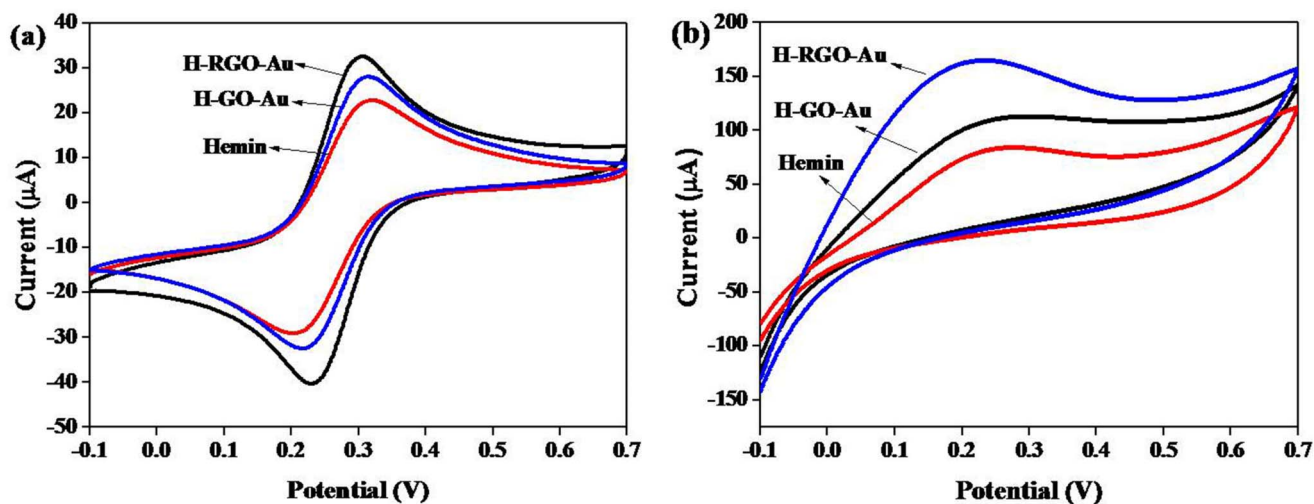


Figure 7 | CVs of H-RGO-Au, H-GO-Au and hemin-modified Au electrodes. (a) Phosphate buffer (pH 7.4) containing 5 mM $K_3Fe(CN)_6$. (b) N_2 -saturated phosphate buffer (pH 7.4) containing 5 mM H_2O_2 .

decomposition of hydrogen peroxide are performed in order to explore the mechanism. From these experimental results, we find that the ternary composite has the highest catalytic activity than that of three components alone or the mixture of three components at the same condition. The excellently catalytic performance of the ternary composite could be attributed to the fast electron transfer on the surface of graphene and the synergistic interaction of three components. The kinetics and thermodynamics of H_2O_2 decomposition by H-RGO-Au indicate that it was superior to the other reported catalysts, which might be also ascribed to the synergistic interaction. The substrates could be absorbed effectively on the surface of H-RGO-Au due to the high surface-to-volume ratio of graphene. Then, the active sites of the gold NPs and hemin absorbed on graphene sheets might react with substrates more directly. This mechanism is similar to that of natural enzymes in which the extraordinarily high catalytic efficiency is largely due to the ability to bring substrates into proximity with their active sites⁴⁸. Furthermore, the electrochemical experiments show that an interleaved electron transfer highways could be built up in H-RGO-Au due to the introduction of graphene. Therefore, we conclude that the excellent peroxidase-like activity of H-RGO-Au could be attributed to the high conductivity and the synergistic interaction of three components.

In summary, we have prepared a new catalyst H-RGO-Au by a simple process. The most important discovery is that H-RGO-Au shows a higher catalytic activity for decomposition of hydrogen peroxide than that of three components alone or the mixture of three components. Kinetic and thermodynamic analysis indicates that the catalytic activity of H-RGO-Au was higher than that of other reported catalysts. The high catalytic activity of H-RGO-Au could be attributed to its high conductivity and the synergistic interaction of three components. At last, the as-prepared H-RGO-Au was used

to determine hydrogen peroxide concentration in three real water samples with satisfactory results. Furthermore, H-RGO-Au is a promising candidate as enzyme mimics with advantages of easy preparation, low-cost, and stability. We envision that the engineered catalytic graphene-based material will hold great promises in potential applications, such as biocatalyst, nanosensors and molecular carriers.

Methods

Synthesis of H-RGO-Au and H-GO-Au. The synthesis of GO was described in our previous reports^{13,14,22}. H-RGO was prepared according to the literature⁴⁹. Briefly, GO (50 mg) was loaded in a 500 mL dried four-necked flask, and 200 mL of H_2O was then added. After stirring and ultrasonication for 30 min, 300 μL of ammonia solution and 50 mg of hemin were added to the mixture, followed by the addition of 50 μL of hydrazine solution. The solution was heated in a water bath at 60 °C for 4 h. The final product was filtered and washed with water for several times and dried in vacuo to obtain H-RGO. Additionally, the preparation of H-GO was similar to H-RGO except no adding hydrazine. H-RGO-Au/H-GO-Au was synthesized by reduction $HAuCl_4$ with ascorbic acid (AA) in the presence of H-RGO/H-GO at room temperature based on a simple and conveniently wet-chemical method. In the process, AA (0.1 M) was added into the premixed solution of $HAuCl_4$ (0.06 mM) and H-RGO/H-GO (6 $\mu g mL^{-1}$) at room temperature for 5 min. This stable H-RGO-Au/H-GO-Au solution was dialyzed overnight to remove excess AA, $HAuCl_4$ and other byproduct.

Kinetic and thermodynamic analysis. Kinetic measurements were carried out in time course mode by monitoring the absorbance change at 652 nm on a TU-1901 UV-Vis spectrophotometer. Catalytic experiments were performed using 0.5 $\mu g mL^{-1}$ of H-RGO-Au in a reaction volume of 600 μL acetic acid-sodium acetate buffer solution (0.02 M, pH 4, 25 °C) with 600 μM TMB as substrate, or 10 mM H_2O_2 , unless otherwise stated. The Michaelis-Menten constant was calculated using the Lineweaver-Burk plot: $1/v = K_m/V_m(1/[S] + 1/K_m)$ where v is the initial velocity, V_m represents the maximal reaction velocity, $[S]$ corresponds to the concentration of substrate and K_m is the Michaelis constant.

Thermodynamics measurements were carried out by fitting the absorbance data of different temperatures to pseudo-first-order kinetics: $y = y_0 + y_1 e^{-kt}$, where k is the reaction rate constant. The value of E_a and A was calculated using the Arrhenius equation: $\ln k = \ln A - E_a/RT$, where A is pre-exponential factor, E_a is the apparent activation energy, R is the ideal gas constant, T is the absolute temperature. The entropy of activation (ΔS) was obtained according to the equation: $\ln A = \Delta S/R$.

Preparation of catalyst-modified electrode. Prior to modification, the gold electrode ($\Phi = 2$ mm) was polished with 0.3 and 0.05 μm alumina slurry, rinsed thoroughly with doubly distilled water between each polishing step, then washed successively with 1 : 1 nitric acid, ethanol, and doubly distilled water in an ultrasonic bath and dried in air. Then 10 μL of H-RGO-Au (3 $\mu g mL^{-1}$) dispersion was dropped onto the Au electrodes to prepare catalyst-modified electrodes. Then the electrodes were dried naturally overnight. 2 μL of the 0.5% Nafion in ethanol was spread on the H-RGO-Au/gold surface as a binder to hold the film on the electrode surface stably. The H-GO-Au/gold electrode and hemin/gold electrode were prepared in the same way by using H-GO-Au and hemin instead of H-RGO-Au. The electrochemically active surface area was calculated by the following formula. $I_p/A = (2.69 \times 10^5) \cdot n^{3/2} \cdot D_0^{1/2}$

Table 3 | Determination of H_2O_2 in water samples ($n = 3$)

Water	Added (μM)	Detection (μM)	Recovery (%)	RSD (%)
Tap water	10	9.97	99.7	1.6
	20	20.04	100.2	0.9
	30	30.44	101.5	1.6
Lake water	10	10.26	102.6	2.7
	20	19.74	98.7	2.3
	30	30.94	103.1	1.3
Commercial water	10	10.26	102.6	1.1
	20	20.21	101.1	1.5
	30	30.44	101.5	0.6



$\cdot C_0^* v^{1/2}$. Where I_p is the peak current, the stoichiometric number of electrons involved in the electrode reaction, $n = 1$, the diffusion coefficient of $K_3Fe(CN)_6$, $D_0 = 0.76 \times 10^{-5} \text{ cm}^2 \text{ s}^{-1}$, the concentration of $K_3Fe(CN)_6$, $C_0^* = 5 \text{ mM}$, v is the scan rate.

Electrochemical measurements were performed on an electrochemical workstation (CHI660C, CH Instrument, USA). The three-electrode system consisted of a platinum wire as auxiliary electrode and an Ag/AgCl (saturated KCl) as reference. Working electrodes were the nanomaterials-modified gold electrodes. All of the electrochemical experiments were carried out at room temperature and ambient pressure.

H₂O₂ detection was realized as follows. A series of different concentrations of H₂O₂ were prepared. 300 μL of TMB (1200 μM), 100 μL of H-RGO-Au (3 $\mu\text{g mL}^{-1}$) stock solution were added to 200 μL of H₂O₂. The mixed solution was used to perform the time course measurement at the wavelength of 652 nm.

H₂O₂ detection in water samples. H₂O₂ solutions of 30, 60, 90 μM were prepared with three different water samples: tap water from laboratory, lake water from Fulong Lake, and commercial water from supermarket, respectively. No other pretreatment process was performed before the use of three water samples. Experiments were carried out by adding 300 μL of TMB (1200 μM) and 100 μL of H-RGO-Au (3 $\mu\text{g mL}^{-1}$) dispersion to 200 μL of H₂O₂ solution prepared with three different water samples. Then the absorption at 652 nm of mixed solution was measured at different times. Every experiment was carried out for three times parallelly.

- Gao, L. Z. *et al.* Intrinsic peroxidase-like activity of ferromagnetic nanoparticles. *Nat. Nanotechnol.* **2**, 577–583 (2007).
- Song, Y. J., Qu, K. G., Zhao, C., Ren, J. S. & Qu, X. G. Graphene oxide: intrinsic peroxidase catalytic activity and its application to glucose detection. *Adv. Mater.* **22**, 2206–2210 (2010).
- Bonar-Law, R. P. & Sanders, J. K. Polyol recognition by a steroid-capped porphyrin. Enhancement and modulation of misfit guest binding by added water or methanol. *J. Am. Chem. Soc.* **117**, 259–271 (1995).
- Zhang, G. F. & Dasgupta, P. K. Hematin as a peroxidase substitute in hydrogen peroxide determinations. *Anal. Chem.* **64**, 517–522 (1992).
- Xue, T. *et al.* Graphene-supported hemin as a highly active biomimetic oxidation catalyst. *Angew. Chem.* **124**, 3888–3891 (2012).
- Wang, Q. G. *et al.* A Supramolecular-hydrogel-encapsulated hemin as an artificial enzyme to mimic peroxidase. *Angew. Chem. Int. Ed.* **46**, 4285–4289 (2007).
- Yamaguchi, H., Tsubouchi, K., Kawaguchi, K., Horita, E. & Harada, A. Peroxidase activity of cationic metalloporphyrin-antibody complexes. *Chem. Eur. J.* **10**, 6179–6186 (2004).
- Novoselov, K. S. *et al.* Electric field effect in atomically thin carbon films. *Science* **306**, 666–669 (2004).
- Du, J. *et al.* Hierarchically ordered macro-Mesoporous TiO₂-graphene composite films: improved mass transfer, reduced charge recombination, and their enhanced photocatalytic activities. *ACS nano* **5**, 590–596 (2010).
- Rafiee, M. A. *et al.* Enhanced mechanical properties of nanocomposites at low graphene content. *ACS nano* **3**, 3884–3890 (2009).
- Stoller, M. D., Park, S., Zhu, Y. W., An, J. H. & Ruoff, R. S. Graphene-based ultracapacitors. *Nano Lett.* **8**, 3498–3502 (2008).
- Guo, C. X. *et al.* Layered graphene/quantum dots for photovoltaic devices. *Angew. Chem. Int. Ed.* **49**, 3014–3017 (2010).
- Dong, J., Ding, J. B., Weng, J. & Dai, L. Z. Graphene enhances the shape memory of poly (acrylamide-co-acrylic acid) grafted on graphene. *Macromol. Rapid Commun.* **34**, 659–664 (2013).
- Yang, Q., Wang, Z. B. & Weng, J. Self-assembly of natural tripeptide glutathione triggered by graphene oxide. *Soft Matter* **8**, 9855–9863 (2012).
- Tao, A., Sinsersuksakul, P. & Yang, P. D. Tunable plasmonic lattices of silver nanocrystals. *Nat. Nanotechnol.* **2**, 435–440 (2007).
- Kong, B. *et al.* Sensitive and selective colorimetric visualization of cerebral dopamine based on double molecular recognition. *Angew. Chem.* **123**, 1877–1880 (2011).
- Huang, X. H., El-Sayed, I. H., Qian, W. & El-Sayed, M. A. Cancer cells assemble and align gold nanorods conjugated to antibodies to produce highly enhanced, sharp, and polarized surface Raman spectra: a potential cancer diagnostic marker. *Nano Lett.* **7**, 1591–1597 (2007).
- Schrinner, M. *et al.* Single nanocrystals of platinum prepared by partial dissolution of Au-Pt nanoalloys. *Science* **323**, 617–620 (2009).
- Jv, Y., Li, B. X. & Cao, R. Positively-charged gold nanoparticles as peroxidase mimic and their application in hydrogen peroxide and glucose detection. *Chem. Commun.* **46**, 8017–8019 (2010).
- Xu, J. *et al.* Gold nanoparticles bound on microgel particles and their application as an enzyme support. *Nanotechnology* **18**, 265704 (2007).
- Karim, Z., Adnan, R. & Ansari, M. S. Low concentration of silver nanoparticles not only enhances the activity of horseradish peroxidase but alter the structure also. *PLoS one* **7**, e41422 (2012).
- Dong, J., Weng, J. & Dai, L. Z. The effect of graphene on the lower critical solution temperature of poly (N-isopropylacrylamide). *Carbon* **52**, 326–336 (2012).
- Meyer, J. C. *et al.* The structure of suspended graphene sheets. *Nature* **446**, 60–63 (2007).

- Hernandez, Y. *et al.* High-yield production of graphene by liquid-phase exfoliation of graphite. *Nat. Nanotechnol.* **3**, 563–568 (2008).
- Li, D., Mueller, M. B., Gilje, S., Kaner, R. B. & Wallace, G. G. Processable aqueous dispersions of graphene nanosheets. *Nat. Nanotechnol.* **3**, 101–105 (2008).
- Zhang, J. L. *et al.* Reduction of graphene oxide vial-ascorbic acid. *Chem. Commun.* **46**, 1112–1114 (2010).
- Gao, J. *et al.* Environment-friendly method to produce graphene that employs vitamin C and amino acid. *Chem. Mater.* **22**, 2213–2218 (2010).
- Stankovich, S. *et al.* Synthesis of graphene-based nanosheets via chemical reduction of exfoliated graphite oxide. *Carbon* **45**, 1558–1565 (2007).
- Marquez, L. A. & Dunford, H. B. Mechanism of the oxidation of 3, 5, 3', 5'-tetramethylbenzidine by myeloperoxidase determined by transient- and steady-state kinetics. *Biochemistry* **36**, 9349–9355 (1997).
- Feng, D. W. *et al.* Zirconium-metalloporphyrin PCN-222: mesoporous metal-organic frameworks with ultrahigh stability as biomimetic catalysts. *Angew. Chem.* **124**, 10453–10456 (2012).
- Song, Y. J., Qu, K. G., Xu, C., Ren, J. S. & Qu, X. G. Visual and quantitative detection of copper ions using magnetic silica nanoparticles clicked on multiwalled carbon nanotubes. *Chem. Commun.* **46**, 6572–6574 (2010).
- Tao, Y., Lin, Y. H., Huang, Z. Z., Ren, J. S. & Qu, X. G. Incorporating Graphene Oxide and Gold Nanoclusters: A Synergistic Catalyst with Surprisingly High Peroxidase-Like Activity Over a Broad pH Range and its Application for Cancer Cell Detection. *Adv. Mater.* **25**, 2594–2599 (2013).
- Wang, Z. B., Lv, X. C. & Weng, J. High peroxidase catalytic activity of exfoliated few-layer graphene. *Carbon* **62**, 51–60 (2013).
- Huang, C. P., Huang, Y. F., Cheng, H. P. & Huang, Y. H. Kinetic study of an immobilized iron oxide for catalytic degradation of azo dye reactive black B with catalytic decomposition of hydrogen peroxide. *Catal. Commun.* **10**, 561–566 (2009).
- Hasnat, M. A. *et al.* Efficient hydrogen peroxide decomposition on bimetallic Pt-Pd surfaces. *Catal. Commun.* **12**, 286–291 (2010).
- Ma, Y., Meng, S., Qin, M., Liu, H. & Wei, Y. New insight on kinetics of catalytic decomposition of hydrogen peroxide on ferrihydrite: Based on the preparation procedures of ferrihydrite. *J. Phys. Chem. Solids* **73**, 30–34 (2012).
- Narayanan, R. & El-Sayed, M. A. Shape-dependent catalytic activity of platinum nanoparticles in colloidal solution. *Nano Lett.* **4**, 1343–1348 (2004).
- Zhu, Y. W. *et al.* Graphene and graphene oxide: synthesis, properties, and applications. *Adv. Mater.* **22**, 3906–3924 (2010).
- Bai, H., Li, C. & Shi, G. Q. Functional composite materials based on chemically converted graphene. *Adv. Mater.* **23**, 1089–1115 (2011).
- Jia, J., Sun, L. P., Hu, N., Huang, G. M. & Weng, J. Graphene enhances the specificity of the polymerase chain reaction. *Small* **8**, 2011–2015 (2012).
- Weng, J. *et al.* Gold-cluster sensors formed electrochemically at boron-doped-diamond electrodes: detection of dopamine in the presence of ascorbic acid and thiols. *Adv. Funct. Mater.* **15**, 639–647 (2005).
- Li, X. R. *et al.* Synthesis of potassium-modified graphene and its application in nitrite-selective sensing. *Adv. Funct. Mater.* **22**, 1981–1988 (2012).
- Li, Y., Zhang, J. J., Xuan, J., Jiang, L. P. & Zhu, J. J. Fabrication of a novel nonenzymatic hydrogen peroxide sensor based on Se/Pt nanocomposites. *Electrochem. Commun.* **12**, 777–780 (2010).
- Zhou, K. F. *et al.* A novel hydrogen peroxide biosensor based on Au-graphene-HRP-chitosan biocomposites. *Electrochim. Acta* **55**, 3055–3060 (2010).
- Xu, J., Liu, C. H. & Wu, Z. F. Direct electrochemistry and enhanced electrocatalytic activity of hemoglobin entrapped in graphene and ZnO nanosphere composite film. *Microchim. Acta.* **172**, 425–430 (2011).
- Li, M. G. *et al.* Direct electrochemistry of horseradish peroxidase on graphene-modified electrode for electrocatalytic reduction towards H₂O₂. *Electrochim. Acta* **56**, 1144–1149 (2011).
- Dato, A., Radmilovic, V., Lee, Z., Phillips, J. & Frenklach, M. Substrate-free gas-phase synthesis of graphene sheets. *Nano Lett.* **8**, 2012–2016 (2008).
- Viloca, M. G., Gao, J. L., Karplus, M. & Truhlar, D. G. How enzymes work: analysis by modern rate theory and computer simulations. *Science* **303**, 186–195 (2004).
- Guo, Y. J. *et al.* Hemin-graphene hybrid nanosheets with intrinsic peroxidase-like activity for label-free colorimetric detection of single-nucleotide polymorphism. *ACS nano* **5**, 1282–1290 (2011).

Acknowledgments

This work is supported by the National Basic Research 973 Project (2014CB932004), National Natural Science Foundation of China (31371005, 81171453), the Knowledge Innovation Program of Shenzhen City (JCY20130327150937484), the Fundamental Research Funds for the Central Universities, Program for New Century Excellent Talents in University, the Ministry of Education, and Open Research Fund of State Key Laboratory of Polymer Physics and Chemistry, Changchun Institute of Applied Chemistry, Chinese Academy of Sciences.

Author contributions

J.W. conceived the work. X.C.L. performed the experiments. All authors analysed the data and prepared the manuscript.



Additional information

Supplementary information accompanies this paper at <http://www.nature.com/scientificreports>

Competing financial interests: The authors declare no competing financial interests.

How to cite this article: Lv, X.C. & Weng, J. Ternary Composite of Hemin, Gold Nanoparticles and Graphene for Highly Efficient Decomposition of Hydrogen Peroxide. *Sci. Rep.* 3, 3285; DOI:10.1038/srep03285 (2013).



This work is licensed under a Creative Commons Attribution-NonCommercial-NoDerivs 3.0 Unported license. To view a copy of this license, visit <http://creativecommons.org/licenses/by-nc-nd/3.0>